```
@article{ruh2023fast,
  author = {Marius L. Ruh and John T. Hwang},
  title = {Fast and Robust Computation of Optimal Rotor Designs Using Blade Element
    Momentum Theory},
  journal = {AIAA Journal},
  year = {2023},
  volume = {61},
  number = {9},
  pages = {4096-4111},
  doi = {10.2514/1.j062611},
  url = {https://doi.org/10.2514/1.j062611}
}
```

Fast and robust computation of optimal rotor designs using blade element momentum theory *

Marius L. Ruh[†] and John T. Hwang[‡]

University of California San Diego, La Jolla, CA, 92093

Abstract

Recent years have seen a renewed interest in rotary-wing aircraft, due to the emergence of urban air mobility. In the conceptual design of such aircraft, fast estimation of rotor performance is important. A challenge is that rotor performance models require a detailed description of the blade geometry, which is not always available at this stage. We have developed a new, robust method for rapidly computing optimal rotor designs, which is derived from blade element momentum theory. In this paper, we derive the rotor design method and prove its convergence for all reasonable model inputs. We verify the design method by comparing the optimal rotor designs it computes to those found by a nonlinear programming algorithm. Thousands of numerical experiments yield relative errors of less than 12% and 4% in terms of the chord and twist profiles, respectively, and less than 0.3% in terms of efficiency, thrust, torque, and power coefficients. In addition, the design method computes optimal designs 200 times faster compared to the nonlinear programming algorithm. Based on these findings, we expect this new rotor design method to be useful in the conceptual design of rotary-wing aircraft.

*Parts of this paper were originally presented at the *AIAA AVIATION 2021 FORUM* held virtually August 2-6, 2021. Paper number: AIAA 2021-2598 `https://doi.org/10.2514/6.2021-2598`

†PhD Student, Department of Mechanical and Aerospace Engineering

‡Assistant Professor, Department of Mechanical and Aerospace Engineering

Nomenclature

V_x	=	axial freestream velocity
u_x	=	axial induced velocity at the rotor disk
a_x	=	axial induction factor
V_θ	=	rotational velocity of the rotor
u_θ	=	rotational induced velocity at the rotor disk
a_θ	=	tangential induction factor
W	=	resultant inflow velocity
Ω	=	rotor rotational speed (rad/s)
ω	=	wake rotational speed (rad/s)
R	=	rotor radius
r	=	radial distance from the rotor hub
S	=	area swept by the rotor
θ	=	sectional blade twist angle
α	=	sectional angle of attack
ϕ	=	sectional inflow angle
c	=	sectional chord length
σ	=	sectional blade solidity
T, C_T	=	thrust, coefficient
Q, C_Q	=	torque, coefficient
P, C_P	=	power, coefficient
J	=	advance ratio
η	=	total efficiency
η_1	=	efficiency for axial induced losses
η_2	=	efficiency for tangential induced losses
FM	=	figure of merit

1 Introduction

Urban air mobility (UAM) aims to enable on-demand and affordable transportation in metropolitan areas using electric aircraft with vertical takeoff and landing (eVTOL) capabilities. Market studies [1, 2] show that the UAM industry could be profitable by 2030. The excitement and envisioned potential surrounding UAM has motivated significant research in a number of relevant areas, including design methods for these eVTOL vehicles.

In the conceptual design and sizing of UAM aircraft, one of the necessary tools is a fast and robust method for the prediction of rotor aerodynamic performance. The blade element momentum (BEM) method is widely used at this stage of the design process due to its computational efficiency and reasonable accuracy for simple operating conditions (i.e., axial inflow). For UAM aircraft, these operating conditions arise during cruise and vertical flight, depending on the aircraft configuration. The lift-plus-cruise configuration (see e.g., [3]) has separate rotors for the vertical and forward flight segments. In this case, BEM theory provides a good option for modeling the lift rotors in hover and the propellers in cruise as the blades are mostly exposed to axial flight. One challenge is that BEM theory requires a detailed description of the rotor geometry, specified by a blade twist and chord distribution. Such information is typically not available at this design stage.

This paper presents a fast and robust rotor design method based on BEM theory, called the BEM-based ideal-loading design (BILD) method. The goal is to compute the optimal blade twist and chord distributions that minimize aerodynamic losses given a small number of design inputs. The optimal rotor geometry is parameterized in terms of a reference chord length at a specified radial location, an airfoil polar, and an operating condition given by advance ratio.

We document several steps that establish this new design method. First, we formulate a rotor design optimization problem and apply the calculus of variations to derive a first-order necessary condition for optimality. Results show that rotors, operating such that this condition is satisfied, minimize aerodynamic losses. Second, we propose a method for finding a solution of the first-order condition, given by expressions for the rotor induced velocities in terms of an intermediate efficiency term that captures rotational momentum losses. We also present equations that allow for the back-computation of the optimal twist and chord profiles. Third, we prove that our method can always find an optimal blade design for reasonable model inputs. Fourth, based on the results of thousands of numerical experiments, we verify that optimal blade geometries computed by the BILD method agree with those found by a nonlinear programming algorithm.

The remainder of this paper proceeds as follows. We first present a literature survey in Sec. 2, summarizing research on blade element momentum theory and optimal rotor design approaches. Then, in Sec. 3, we review classical BEM theory. If the reader is already familiar with BEM methods, we recommend moving to Sec. 4, where we derive the BILD method. Lastly, in Sec. 5, we present the results of this research effort.

2 Literature Survey

2.1 Blade element momentum theory

Blade element momentum (BEM) methods are widely used in the low-fidelity analysis of rotors and wind turbines. Madsen et al. [4, 5] compared BEM results with numerical actuator disk (AD) simulations and found close correlation between the overall performance predictions of rotors using the two methods. Similarly, Gur [6] found that in steady, level flight, higher-fidelity methods such as lifting-line theory or vortex methods do not offer an advantage over BEM methods, which are computationally more efficient. Despite its computational efficiency and reasonable accuracy for axial flow, blade element momentum theory has several limitations. Bontempo and Manna [7–10] extensively investigated errors introduced in momentum theory by comparing results of BEM with AD simulations and found two main sources of errors. The first error stems from replacing the integral form of the equations with the differential form. The second error is due to the linearization of the angular blade velocity in the derivation of the angular momentum balance. Due to these errors, BEM theory predicts the local induced velocities incorrectly in the hub and tip regions.

Numerous efforts have been made to improve BEM methods. One area of improvement has been the modeling of aerodynamic losses near the hub and tip, first addressed by Glauert [11], who introduced the original formulation of the Prandtl tip-loss factor. Shen et al. [12] analyzed various formulations of the Prandtl tip-loss function and proposed a new tip-loss model to address inconsistencies in previous implementations. Branlard and Gaunaa [13] also developed a tip-loss correction model, based on vortex theory. Other areas where BEM has been improved include low-Reynolds number flow [14–16], modeling large angles of attack and post-stall behavior [17–20], applications for coned rotors [21] as well as slipstream and wake modeling [22–25].

Lastly, an important consideration in the implementation of BEM theory is robustness. Combining blade element and momentum theory leads to a residual that needs to be solved numerically and robust convergence is important, particularly in multidisciplinary design optimization. Shen et al. [26] investigated the convergence of fixed-point iterative schemes to solve the BEM equations and proposed an improved version. Masters et al. [27] proposed a robust numerical scheme based on Monte Carlo simulations and sequential quadratic optimization. Ning [28, 29] showed how to parameterize the residual in terms of a single variable by introducing a minor approximation, reducing the problem to a one-dimensional root finding algorithm with guaranteed convergence.

2.2 Optimal rotor design

2.2.1 Minimum induced loss methods

Minimum induced loss (MIL) methods are low-fidelity, inverse design approaches that compute the optimal rotor geometry for a desired thrust or power coefficient, by leveraging the Betz (1919) [30] condition for minimum induced loss. The Betz condition states that a rotor's maximum efficiency is achieved when the circulation along the blade sheds a rigid, helicoidal vortex sheet that moves downstream along the rotor axis at constant velocity. This condition primarily holds for lightly loaded propellers but Theodorsen [31] was able to extend it to heavily loaded rotors, by considering the contraction of the slipstream. A design method based on the Betz condition was first introduced by Larrabee [32] and refined by Adkins and Liebeck [33] to correct small angle approximations, improve accuracy, and account for viscous terms. To start the design process, an initial value for the displacement velocity ratio needs to be specified. This is the ratio between the velocity of the helicoidal vortex-sheet to the freestream velocity. Adkins and Liebeck [33] state that a value of zero is acceptable. The optimal blade shape is computed iteratively until the design produces a displacement velocity ratio that matches the initial value as well as the desired thrust or power coefficient. According to Adkins and Liebeck, the method is expected to converge in less than five iterations. However, convergence issues exist for off-design conditions, which can occur near the blade tip due to large values of the induction factors, which relate the inflow angle and displacement velocity ratio. There exist numerous variations [34–40] of the MIL design approach, all of which leverage the Betz condition.

2.2.2 Other rotor design methods

An alternative approach to optimal rotor design is to numerically solve an optimization problem to maximize or minimize an objective function (e.g., efficiency or torque) with respect to the rotor geometry. One optimization strategy is the calculus of variations, which was used as early as the 1940s [41, 42] to optimize the blade twist distribution of existing rotor designs. In a more recent paper (2015), Dorfling and Rokhsaz [43] proposed a method for deriving and solving the Euler–Lagrange equations to perform a blade twist optimization. They used a combination of blade element and vortex theory as their aerodynamic model.

A more common approach for optimizing rotor blade geometries is to use nonlinear programming algorithms. Chang and Sullivan [44] used a penalty method developed by Fiacco and McCormick [45] to find the optimal twist distribution for maximizing efficiency of general aviation propellers subject to a constant power constraint. Results show an improvement of 1-6% in ideal efficiency. A similar study was conducted by Chang and Stefko [46] to optimize the twist distribution of two NACA propellers operating at higher Mach numbers (up to 0.71), using the same penalty method for optimization. The authors found no significant improvement in rotor efficiency at these higher Mach numbers. Cho and Lee [47] used the extended linear interior penalty function method to optimize the chord and twist distribution of multiple SR and NACA rotors. The best improvement in efficiency was 2.3% for the SR-2 rotor. Lastly, Burger et al. [48] optimized the number of blades, sweep angle, and airfoil shape, in addition to the twist and chord distribution for two rotors, using a genetic algorithm. All prior work mentioned in this paragraph used the vortex lattice method (VLM) for aerodynamic prediction.

3 Review of classical blade element momentum theory

We present the BEM equations in a form that applies to both zero and non-zero normal inflow. Conventional implementations do not work under zero inflow conditions due to the use of normalized induction factors, which have a singularity at zero normal inflow. For brevity, we do not include tip loss factors in the presentation of the BEM equations. However, for all results shown in this paper, Prantdl's formulation for tip losses was used. Figure 1 shows the geometric interpretation of BEM theory.

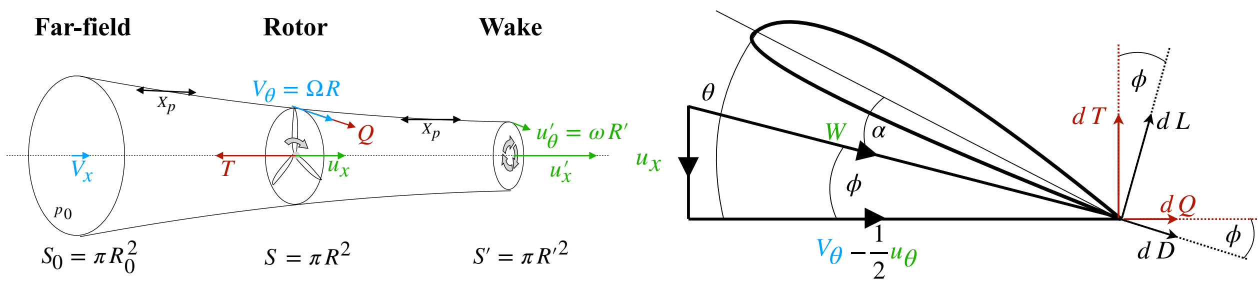

(a) Streamtube for momentum theory

(b) Blade element analysis

Figure 1: Geometry for blade element momentum theory

3.1 Momentum Theory

Momentum theory predicts the performance of a rotor by analyzing the change in momentum of the air in the axial and tangential direction. The rotor is modeled as an actuator disk and its effect is confined to a control volume, called streamtube. By considering the increase in axial momentum only, the equation for sectional thrust can be derived as

$$dT = 4\pi\rho u_x \left(u_x - V_x\right) r\, dr = 4\pi\rho V_x^2 \left(1 + a_x\right) a_x r\, dr, \tag{1}$$

where the axial induced velocity u_x is related to the axial induction factor as $u_x = V_x(1 + a_x)$. It is clear that Eq. (1) in terms of a_x is undefined when $V_x = 0$, which is not the case when using the non-normalized form. A similar expression for sectional thrust can be derived by modeling the increase in pressure across the actuator disk in terms of the tangential induced velocities, using

Bernoulli's principle. The expression is shown in Tab. 1, denoted $d\tilde{T}$. Next, the equation for sectional torque can be derived by considering the increase in angular momentum of the air behind the rotor disk. The result is

$$dQ = 2\pi\rho u_x u_\theta r^2 dr = 4\pi\rho V_x V_\theta \left(1 + a_x\right) a_\theta r^2 \, dr, \tag{2}$$

where a_θ is the tangential induction factor, defined by Glauert [11] as $a_\theta = u_\theta/2V_\theta$. Like Eq. (1), the torque equation in terms of the induction factors is undefined for zero normal inflow. The axial and tangential induced velocities u_x and u_θ are sources of aerodynamic inefficiencies, which can be expressed as

$$\eta_1 = \frac{V_x}{u_x}, \quad \text{and} \quad \eta_2 = \frac{V_\theta - {}^{u_\theta}/_{2}}{V_\theta}, \tag{3}$$

where η_1 and η_2 capture the axial and rotational induced losses, respectively. More details on the derivation of these expressions and momentum theory in general can be found in a conference paper by the authors [49].

3.2 Blade element theory

In blade element theory, we discretize the rotor blade radially, treating each blade element as an infinitesimally thin 2-D airfoil, as shown in Fig. 1b. For the results shown in this paper, we neglect compressibility effects and model the lift and drag coefficients as functions of the angle of attack and Reynolds number, such that

$$C_l = f\left(\alpha, Re\right) \quad \text{and} \quad C_d = g\left(\alpha, Re\right). \tag{4}$$

For our numerical experiments (Sec. 5), we use a surrogate modeling technique called regularized minimal-energy tensor-product splines (RMTS) [50, 51] to establish the relationships in Eq. (4). To generate the training dataset, we use XFOIL [52] to predict lift and drag coefficients at various combinations of α and Reynolds number and apply the Viterna method [19] to extrapolate the airfoil polar to $\alpha = \pm 90°$. This extrapolation ensures that the model is well-defined for any angle of attack, which is important during optimization. To guarantee a smooth transition between the pre and post-stall regimes, we apply a cubic smoothing function to the transition region. More information on the training data and the smoothing function can be found in Appendix 7.2. Next, the inflow geometry shown in Fig. 1b can be used to write the thrust and torque as

$$dT = dL\cos\phi - dD\sin\phi = \frac{1}{2}C_x\rho W^2 Bcdr, \tag{5}$$

$$dQ = dL\sin\phi + dD\cos\phi = \frac{1}{2}C_\theta\rho W^2 Bcrdr, \tag{6}$$

where, c is the airfoil chord length and C_x, C_θ, and W are given by

$$\begin{bmatrix} C_x \\ C_\theta \end{bmatrix} = \begin{bmatrix} \cos\phi & -\sin\phi \\ \sin\phi & \cos\phi \end{bmatrix} \begin{bmatrix} C_l \\ C_d \end{bmatrix}, \quad \text{and} \quad W = \sqrt{u_x^2 + \left(V_\theta - \frac{1}{2}u_\theta\right)^2}. \tag{7}$$

3.3 Blade element momentum theory

By equating the expressions for thrust (i.e., Eq. (1), Eq. (5)) and torque (i.e., Eq. (2), Eq. (6)) derived from momentum and blade element theory, we can write the induced velocities as

$$u_\theta = \frac{2\sigma C_\theta V_\theta}{4\sin\phi\cos\phi + \sigma C_\theta} \quad \text{and} \quad u_x = V_x + \frac{\sigma C_x V_\theta}{4\sin\phi\cos\phi + \sigma C_\theta}, \tag{8}$$

where C_x and C_θ are given by Eq. (7) and σ is the sectional blade solidity, defined as $\sigma = Bc/(2\pi r)$ for a rotor with B blades. By relating the induced velocities given in Eq. (8) to the inflow geometry shown in Fig. 1b (i.e., $\tan\phi = u_x/(V_\theta - u_\theta/2)$), a residual can be derived, given as

$$R(\phi) = \frac{J}{\pi}\left(\sigma C_\theta + 4\sin\phi\cos\phi\right) + \left(\sigma C_x - 4\sin^2\phi\right). \tag{9}$$

To solve Eq. (9) for ϕ, we need to know the chord and twist distribution, along with the airfoil polar. We solve Eq. (9) via a bracketed search algorithm to determine ϕ. Then, we use Eq. (8) to find the induced velocities, which allows us to use either the blade element or the momentum equations to compute thrust and torque. We summarize the most important equations from blade

Table 1: Summary of blade element momentum theory equations

Theory	Thrust	Torque	Notes
Axial momentum	$dT = 4\pi\rho u_x (u_x - V_x)\, r\, dr$	N/A	assumes that $u_x = \frac{1}{2}(V_x + u_x')$
Angular momentum	$d\tilde{T} = 2\pi\rho \left(V_\theta - \frac{1}{2}u_\theta\right) u_\theta r\, dr$	$dQ = 2\pi\rho u_x u_\theta r^2 dr$	$d\tilde{T}$ derived from Bernoulli
Blade Element	$dT = \frac{1}{2} C_x \rho W^2 B c dr$	$dQ = \frac{1}{2} C_\theta \rho W^2 B c r dr$	Assumes known c and θ profile

element momentum theory in Tab. 1 and present common rotor performance metrics in Tab. 2.

Table 2: Summary of rotor performance metrics

Performance variable	Metric/Coefficient	Notes
Thrust	$C_T = \frac{T}{\rho n^2 D^4}$	n is rotational speed (rev/s), D is rotor diameter
Torque	$C_Q = \frac{Q}{\rho n^2 D^5}$	
Power	$C_P = \frac{P}{\rho n^3 D^5}$	
Efficiency	Forward flight: $\eta = \frac{V_x T}{\Omega Q}$ Hover: $FM = \frac{T}{P}\sqrt{\frac{T}{2\pi R^2 \rho}}$	Ω is rotational speed (rad/s) FM replaces η in hover
Loading	$\frac{T}{S}$ (disk), $\frac{C_T}{\sigma_r}$ (blade)	S is rotor disk area; $\sigma_r = \frac{B \int_0^R c(r) dr}{\pi R^2}$

4 BEM-based ideal-loading design method

In this section, we present a new method for low-fidelity rotor design that is based on blade element momentum (BEM) theory, called the BEM-based ideal-loading design (BILD) method. This method computes the ideal blade chord and twist distributions that minimize the total rotor aerodynamic energy losses given a small number of design inputs. The input variables that need to be specified are the freestream velocity V_x, rotor radius, rotational speed, number of blades, a reference radius at which we assume a chord length c, and the airfoil polar. We present the new theory that underlies the BILD method, which solves the following optimization problem.

Problem 1 (Rotor energy loss minimization)**.** Consider a rotor with a desired thrust T^*. The rotor energy loss minimization problem is

$$\begin{aligned} \underset{u_x}{\text{minimize}} \quad & E[u_x] \\ \text{subject to} \quad & T[u_x] = T^*, \\ & u_x(r_{hub}) = U_{r_{hub}}, \\ & u_x(r_{tip}) = U_{r_{tip}}, \end{aligned} \tag{10}$$

where E and T are functionals given by

$$E\left[u_x\right]=\int_{r_{hub}}^{r_{tip}} E_r\left(r, u_x\right) dr \quad \text{and} \quad T\left[u_x\right]=\int_{r_{hub}}^{r_{tip}} T_r\left(r, u_x\right) dr, \tag{11}$$

representing the total rate of energy loss and total thrust, respectively.

The remainder of this section is organized as follows. First, in Sec. 4.1, we use concepts from the calculus of variations to solve Prob. 1. The solution to this infinite-dimensional optimization problem is given by the ideal-loading condition. Second, in Sec. 4.2, we use the ideal-loading condition to formulate the BILD method by developing equations to compute the induced velocities u_x and u_θ that minimize the overall energy loss. Third, in Sec. 4.3, we show how to back-compute the ideal rotor geometry from the induced velocities.

4.1 Derivation of the ideal-loading condition

In this section, we derive the ideal-loading condition. We want to minimize the rate of energy loss E (i.e., power loss) of a rotor while producing some positive thrust. The definition of the power loss is input power minus output power and can be written as

$$E_r=\Omega Q_r-V_x T_r, \tag{12}$$

where $E_r={}^{dE}/_{dr}$, $Q_r={}^{dQ}/_{dr}$ and $T_r={}^{dT}/_{dr}$. Substituting the expressions for T_r and Q_r from Eq. (1) and Eq. (2), respectively, we write the power loss as

$$E_r=2\pi r\rho\left(V_\theta u_x u_\theta-2V_x u_x^2+2V_x^2 u_x\right). \tag{13}$$

Assumption 1. The rate of energy loss E due to the tangential induced velocity u_θ is negligible.

We see that E_r depends on the radius and the induced velocities which, in turn, depend on the radius. As stated in Assumption 1, we assume that the power loss is primarily due to the axial induced velocity u_x and neglect the effect of rotational losses due to u_θ in the optimization problem. This simplifies the analysis and allows us to write the functionals given by Eq. (11) in terms of u_x

only. Glauert [11] found that according momentum theory, losses due to u_θ are at most 4% for large torque coefficients, confirming that Assumption 1 is reasonable. We now solve Prob. 1.

Lemma 1 (Ideal-loading constant)**.** *Let u_x^* solve Prob. 1. The ideal-loading constant, defined as*

$$\lambda = -\frac{{}^{\partial E_r}/_{\partial u_x}}{{}^{\partial T_r}/_{\partial u_x}}, \tag{14}$$

is constant span-wise, where the partial derivatives are evaluated at u_x^*.

Proof. Problem 1 is a constrained variational problem that can be solved with the method of Lagrange multipliers. A necessary condition for u_x to minimize functional E is that there exists a Lagrange multiplier λ such that u_x satisfies the Euler–Lagrange equation, that is

$$\frac{\partial E_r}{\partial u_x} - \frac{d}{dx}\frac{\partial E_r}{\partial u_x'} + \lambda\left(\frac{\partial T_r}{\partial u_x} - \frac{d}{dx}\frac{\partial T_r}{\partial u_x'}\right) = 0. \tag{15}$$

Formulations of the Euler–Lagrange equations for constrained variational optimization problems like Prob. 1 are treated in various textbooks [53–55]. Here, u_x' is the derivative with respect to the radius (i.e., $u_x' = {}^{du_x}/_{dr}$). Since E_r and T_r are not dependent on u_x', Eq. (15) simplifies to

$$\frac{\partial E_r}{\partial u_x} + \lambda\frac{\partial T_r}{\partial u_x} = 0, \tag{16}$$

and we rearrange to obtain Eq. (14). Since u_x is parameterized in terms of r, Eq. (14) has to hold along the entire rotor span, and therefore the ideal-loading constant λ is constant span-wise. □

Remark 1. Lemma 1 states the first-order necessary condition for optimality for Prob. 1. Results show (see Sec. 5) that if Lemma 1 holds, the corresponding u_x indeed minimizes the total rate of energy loss. Hestenes [56] derived sufficient conditions for optimization problems of this nature, which are also known as "isoperimetric" problems due to the integral equality constraint.

Glauert [11] first established the result of Lemma 1, and Ruh and Hwang [49] applied it to develop the BILD method. However, both approaches relied on a logic-based thought experiment and to the authors' knowledge, this is the first rigorous solution of this problem using the calculus of variations. Next, we derive the analytic expression for λ.

Assumption 2. Each blade element operates at its maximum lift-to-drag ratio.

To derive an analytic expression for λ, we need to evaluate the right-hand side of Eq. (14). Taking the partial derivative of E_r (i.e., Eq. (13)) with respect to u_x leads to

$$\frac{\partial E_r}{\partial u_x} = 2\pi r\rho \left(V_\theta u_\theta + V_\theta u_x \frac{\partial u_\theta}{\partial u_x} - 4V_x u_x + 2V_x^2 \right). \tag{17}$$

To compute $\partial u_\theta / \partial u_x$, we divide the expressions for thrust according to momentum and blade element theory by the corresponding expressions for torque and equate the fractions. The result is

$$\frac{2\left(u_x - V_x\right)}{u_\theta} = \frac{C_l \cos\phi - C_d \sin\phi}{C_l \sin\phi + C_d \cos\phi}. \tag{18}$$

From Assumption 2, we can approximate the right-hand-side as $1/\tan\phi$, which can be expressed in terms of u_x and u_θ according Fig. 1b. This allows us to write $\partial u_\theta / \partial u_x$ as

$$\frac{\partial u_\theta}{\partial u_x} = \frac{2\left(2u_x - V_x\right)}{V_\theta - u_\theta}. \tag{19}$$

We substitute this expression into Eq. (17) to obtain

$$\frac{\partial E_r}{\partial u_x} = 2\pi r\rho \left(V_\theta u_\theta + V_\theta u_x \frac{2\left(2u_x - V_x\right)}{V_\theta - u_\theta} - 4V_x u_x + 2V_x^2 \right). \tag{20}$$

Taking the partial derivative of T_r with respect to u_x is straightforward, and the result is

$$\frac{\partial T_r}{\partial u_x} = 4\pi r\rho \left(2u_x - V_x\right). \tag{21}$$

By substituting the expressions for $\partial E_r / \partial u_x$ and $\partial T_r / \partial u_x$ into Eq. (16), we obtain the analytic form for the ideal-loading constant as

$$\lambda = \frac{V_\theta u_\theta}{2\left(2u_x - V_x\right)} + \frac{V_\theta u_x}{V_\theta - u_\theta} - V_x. \tag{22}$$

Remark 2. To obtain the expression for ${}^{\partial u_\theta}/_{\partial u_x}$ given by Eq. (19), we make the assumption that viscous effects due to blade profile drag are negligible (see Assumption 2). This allows us to express λ in terms of the induced velocities only, which is convenient. Since aerodynamic losses due to u_θ are low, the loss of accuracy when evaluating ${}^{\partial u_\theta}/_{\partial u_x}$ is small. This is supported by the results of a large set of verification studies (see Tab. 3).

Assumption 3. The induced-velocity profiles u_x and u_θ satisfy the following conditions at all span-wise locations, such that

$$0 \leq V_x < u_x \quad \text{and} \quad 0 < u_\theta < V_\theta.$$

Assumption 3 is reasonable for all design conditions. This is because in order to produce positive thrust, the axial induced velocity u_x needs to be larger than the freestream velocity V_x according to momentum theory (see Eq. (1)). The tangential induced velocity u_θ cannot be greater than the angular speed of the rotor blade V_θ. We note that this assumption is trivial in hover. Given Assumption 3, we can easily show that $\lambda > 0$ (see Appendix 7.1).

4.2 Formulation of the BEM-based ideal-loading design method

In this section, we derive equations for the induced velocities u_x and u_θ that minimize the total energy loss per unit time of a rotor. In combination with the result of the ideal-loading condition stated by Eq. (22), these equations form the foundation of the BILD method.

Assuming we know the ideal-loading constant λ, the two unknowns in Eq. (22) are u_x and u_θ. In practice, to determine λ, we apply the BEM equations once at an arbitrary section along the rotor blade. We assume the chord length is given and determine the maximum lift-to-drag ratio ${}^{C_l}/_{C_d}$ based on the airfoil polar of our choice. This allows us to compute u_x and u_θ at that blade section from which we find λ. Now, we rewrite the analytic form of λ, given by Eq. (22), in terms of a single variable that connects u_x and u_θ. This unifying variable is η_2, which we defined earlier in Sec. 3.1 and state again as

$$\eta_2 = \frac{V_\theta - {}^{u_\theta}/_2}{V_\theta}. \tag{23}$$

This can be rearranged to write u_θ in terms of η_2, such that

$$u_\theta = 2V_\theta\left(1 - \eta_2\right). \tag{24}$$

Next, we recall Eq. (18) but do not approximate the right-hand side as $1/\tan\phi$ because we want the induced velocity u_x to capture the effect of blade profile drag. This results in

$$\frac{2\left(u_x - V_x\right)}{u_\theta} = \frac{C_l\left(V_\theta - u_\theta/2\right) - C_d u_x}{C_l u_x + C_d\left(V_\theta - u_\theta/2\right)}. \tag{25}$$

Substituting Eq. (24) into Eq. (25) and solving for u_x leads to

$$u_x = \left(\frac{V_x - V_\theta C_d/C_l}{2}\right) + \sqrt{\left(\frac{V_x - V_\theta C_d/C_l}{2}\right)^2 + \eta_2 V_\theta^2\left(1 - \eta_2 + \frac{V_x}{V_\theta}\frac{C_d}{C_l}\right)}. \tag{26}$$

Remark 3. The inverse of the lift-to-drag ratio appears in Eq. (26). In Assumption 2, we stated that each blade element operates at its maximum lift-to-drag ratio. To investigate the sensitivity of u_x, we plot it as a function of the lift-to-drag ratio for different values of V_x, V_θ, and η_2. Based on the results (see Fig. 10 in Appendix 7.3), increasing C_l/C_d beyond 40 does not significantly change u_x, and a value of C_l/C_d of about 20 will result in values of u_x that are over 90% of the maximum value. Hence, for sufficiently large lift-to-drag ratios, u_x is primarily dependent on V_x, V_θ, and η_2. This is the case for most airfoils that would be used for eVTOL applications. However, for low Reynolds number applications such as micro-UAVs, the maximum lift-to-drag ratio may be low enough such that it significantly affects u_x.

Having established expressions for u_x and u_θ, we can now rewrite the expression for λ given by Eq. (22) in terms of η_2 by substituting Eq. (24) and Eq. (26). After some algebra we obtain a fourth-order polynomial of the form

$$P(\eta_2) = a_4\eta_2^4 + a_3\eta_2^3 + a_2\eta_2^2 + a_1\eta_2 + a_0 = 0, \tag{27}$$

where the polynomial coefficients are in terms of V_x, V_θ, C_l, C_d and λ, and are shown in Appendix

7.2. The roots of this quartic equation represent the local annular efficiency η_2, which can be determined at each blade section using a root finding algorithm. Even though there are four mathematical roots that can be real or complex, Eq. (24) requires that η_2 lies between 0.5 and 1 since the tangential induced velocity cannot be greater than the rotational velocity of the rotor. In practice, only one root satisfies this requirement. Once the distribution of η_2 is found, the induced velocities are calculated via Eq. (24) and Eq. (26) from which thrust and torque are determined using momentum theory. Given thrust or torque, the ideal twist and chord profiles can be back-computed (see Sec. 4.3). Since the goal of the BILD method is to compute the optimal blade geometry, a robust method to compute η_2 is important to make the algorithm reliable.

Algorithm 1 BILD Method

1: Specify advance ratio, airfoil polar, and reference chord length at some span-wise location
2: Perform one BEM analysis (see Sec. 3.3) to find u_x and u_θ at specified span-wise location
3: Compute ideal-loading constant λ using Eq. (22)
4: Solve fourth order polynomial Eq. (27) to find span-wise distribution η_2
5: Compute span-wise distribution of u_x and u_θ from Eq. (26) and Eq. (24); If more than one airfoil is used, estimate $({}^{C_l}\!/_{C_d})_{max}$ for each airfoil when computing u_x
6: Compute thrust and torque from Eq. (1) and Eq. (2)
7: Back-compute ideal rotor geometry (see Sec. 4.3)

Assumption 4. Let $V_x, V_\theta, {}^{L}\!/_{D} > 0$.

Theorem 1 (Convergence of BILD method in axial flow)**.** *If Assumption 4 is satisfied and given that a BEM analysis converges, the BILD algorithm, Alg. 1, is guaranteed to converge.*

Proof. In Alg. 1, we need to show that step 5 always converges. We require η_2 to lie between 0.5 and 1. Evaluating Eq. (27) at these values leads to

$$P(0.5) = -V_\theta^3 \left(\frac{2V_x}{{}^{L}\!/_{D}} + V_\theta \right) \left(V_\theta^2 + V_x^2 \right) \quad \text{and} \tag{28}$$

$$P(1) = V_x V_\theta^2 \lambda \left(\frac{2V_\theta}{{}^{L}\!/_{D}} + V_x \right) \left(\lambda + \frac{2V_\theta}{{}^{L}\!/_{D}} + 2V_x \right). \tag{29}$$

If we can show that $P(0.5)$ and $P(1)$ always have different signs, we guarantee a bracket. Given that $\lambda > 0$, all terms in Eq. (28) are positive, and it follows trivially that $P(0.5) < 0$. Likewise, all terms in Eq. (29) are positive, and $P(1) > 0$. Hence, a bracket always exists, and a bracketed root finding algorithm for η_2 will always converge. Therefore, the BILD method always converges. $\square$

The first part of the hypothesis of Thm. 1 concerns Assumption 4, which is reasonable for most design cases. We know that the ideal-loading constant λ, the lift-to-drag ratio, and the rotational velocity V_θ are always positive for reasonable design condition. Enforcing that the axial inflow velocity V_x is strictly greater than zero is not always reasonable since in hover this is not the case. Of course, to approximate the hover condition one could set V_x to a small number greater than zero. However, we will consider the case of zero axial inflow in more detail. The second part of the hypothesis of Thm. 1 is that a BEM iteration converges. Implementations of BEM methods with provable convergence (e.g., by Ning [28]) exist, and we use a similar implementation in designing the BILD method.

Remark 4 (Convergence of BILD method in hover). It is easy to see that Theorem 3 does not hold when $V_x = 0$. While the lower bound of the bracket (i.e., $P(0.5)$) will always be negative, the upper bound is $P(1) = 0$. This means that the interval $\eta_2 = [0.5, 1]$ is no longer guaranteed to contain a bracket. In this case, $\eta_2 = 1$ is in fact a solution to Eq. (27), which is shown in Appendix 7.2. Since η_2 must be less than 1 there has to be another real root between 0.5 and 1. For polynomials of degree four and lower, it is possible to find an analytic expression for all roots. It turns out that in this case, there exists only one other real root, whose expression can be found in Appendix 7.2. Due to the complicated nature of this equation, it is difficult to derive explicit conditions, for which this root always remains real.

In Fig. 2a, we plot this root as a function of the angular velocity V_θ for different values of the ideal-loading constant λ. The lift-to-drag ratio is set to 20. We see that as λ approaches zero, η_2 approaches one. In Fig. 2b, we plot the quartic polynomial Eq. (27) as a function of the efficiency η_2 for the same values of λ, lift-to-drag ratio, and a rotational speed of $V_\theta = 25$m/s. The plot confirms that a bracketed search algorithm will indeed converge to the analytic roots shown in Fig. 2a. By visual inspection, we can conclude that a bracket still exists within the interval $\eta_2 = [0.5, 1]$ when $V_x = 0$. Therefore, a bracketed root finding algorithm will converge under reasonable design conditions and zero normal inflow.

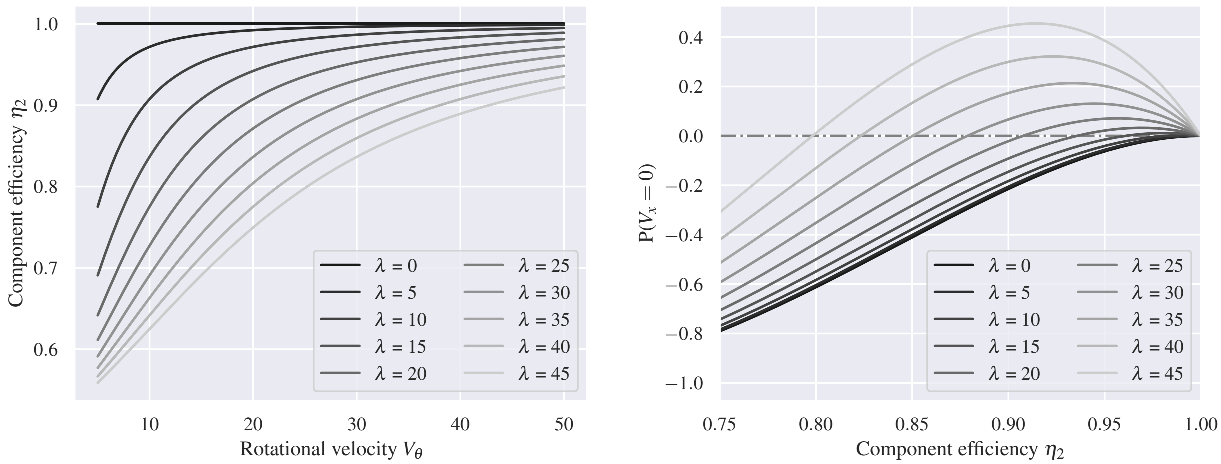

(a) η_2 computed analytically as a function of V_θ (b) Equation (27) as a function of η_2

Figure 2: Visual inspection of the convergence of BILD in hover

4.3 Back-computation of ideal rotor geometry

The last step of the BILD method is the back-computation of the ideal-rotor geometry given by the blade chord and twist distribution. As stated in the previous section, knowing the ideal induced velocities u_x (Eq. (26)) and u_θ (Eq. (24)) allows us to calculate thrust and torque via momentum theory. Now, we want to back-compute the chord and twist distribution. We recall from Fig. 1b that the twist angle is given as $\theta = \phi + \alpha$. Since we know the distributions of the induced velocities u_x and u_θ, we can compute the inflow angle ϕ at each radial section as

$$\phi = \tan^{-1}\left(\frac{u_x}{V_\theta - u_\theta/2}\right). \tag{30}$$

To determine the angle of attack, we make the assumption that α is constant for each airfoil along the blade such that it maximizes the lift-to-drag ratio. This is a reasonable assumption for our model as it aligns well with the ideal-loading analysis. Knowing α and ϕ we can compute the twist angle θ. The computation of the chord is straightforward and involves rearranging either Eq. (5)

or Eq. (6) to isolate chord c. For instance, we can compute c as

$$c = \frac{2dT}{C_x \rho W^2 B dr}. \tag{31}$$

5 Numerical results

5.1 Verification of the BEM-based ideal-loading design method

To verify the BILD method, we use an open-source Python[1] BEM implementation to solve the same optimization problem as the BILD method numerically with the SNOPT [57] algorithm. We solve an energy minimization problem with 30 chord and twist design variables each. In a first study inspired by UAM design, the thrust constraint for the optimization is such that the optimized rotor design produces enough thrust to support the weight (725 kg) of an Airbus Vahana, an electric urban air mobility concept, in hover. The relevant specifications of this aircraft were provided by two studies, investigating UAM design [58, 59]. Figure 3 shows the result of the BEM optimization (blue) and the BILD method (red). We see that the back-computed blade chord and twist distributions, shown in the left column, match the results from the SNOPT optimization reasonably well. We also see that the optimized distributions of the sectional lift and drag coefficients are mostly constant along the span and vary only near the hub and tip. This supports the assumption made in the BILD method that the sectional lift and drag coefficients are constant, such that the lift-to-drag ratio is maximized.

Next, we summarize the results of a large set of verification studies in which we sample the input design space of the BILD method and compare key performance metrics (efficiency, thrust, power, torque coefficient) with those of converged SNOPT BEM optimizations. The setup of the numerical experiments is as follows. We perform a full-factorial sweep of advance ratio (0 to 3), rotor radius (0.5 to 1.5 m), altitude (0 to 3000 m), and reference chord (0.08 to 0.22 m) at a constant RPM of 800 and a normalized reference radius of $r/R = 0.5$. The design space is discretized with ten points in each dimension, equaling 10,000 combinations of the four input variables. For each combination, we

[1] `https://github.com/LSDOlab/lsdo_rotor`

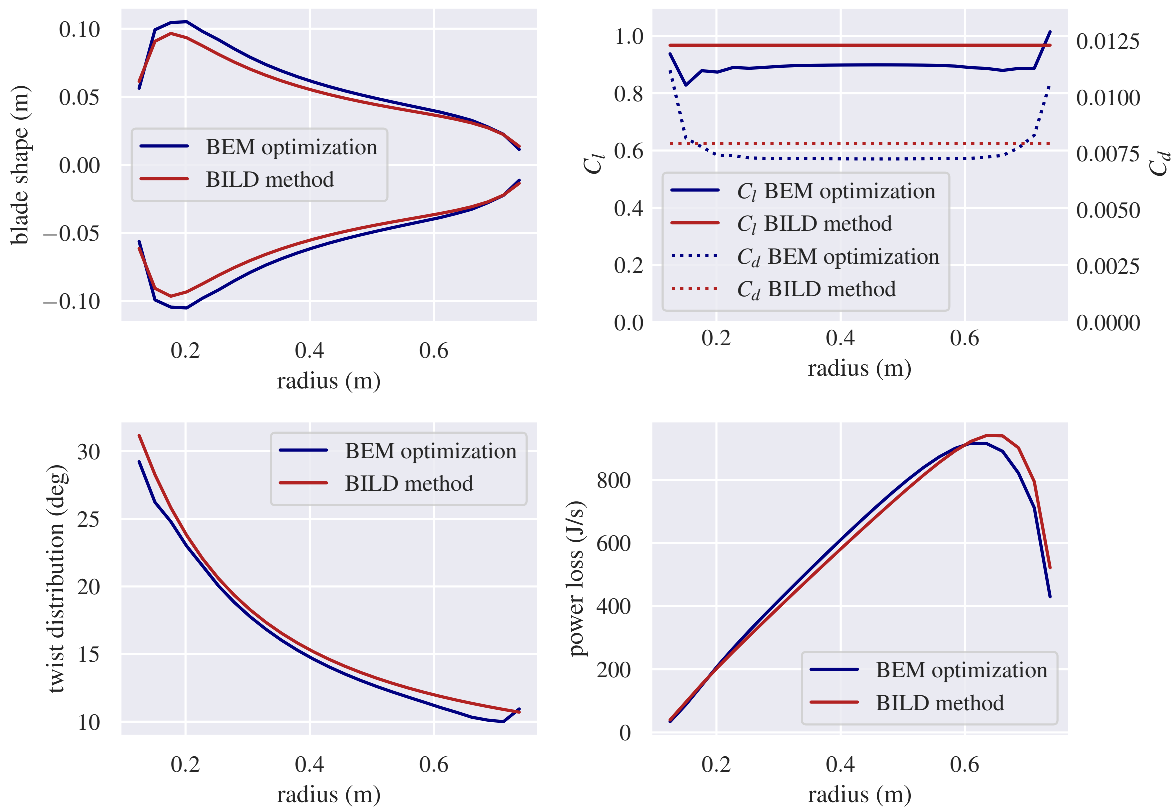

Figure 3: Verification of the BILD method

evaluate the BILD method and use the computed thrust as an equality constraint in the SNOPT optimization. The goal of these numerical experiments is to demonstrate the robustness of the BILD algorithm, its computational efficiency, and reasonable accuracy with respect to high-level performance metrics.

In Fig. 4, we show a scatter plot of the BEM optimization time versus the BILD method. We see that the BILD algorithm is significantly faster than the SNOPT algorithm with an average speed-up in optimization time by a factor of over 200 for converged optimizations. While the SNOPT optimization time is on the order of seconds, which may seem fast, this time can be significant in large-scale multidisciplinary design optimization (MDO) problems that consider rotor analysis and optimization as a subsystem discipline. In addition, about 13% of the SNOPT optimizations did not converge successfully (orange markers) while the BILD method converged in all cases. Convergence failure is of significant concern in large-scale MDO problems as a single failure of a subsystem model can cause the whole system model to also fail. Lastly, in Fig. 5, we plot predictions of aerodynamic efficiency as well as thrust, power and torque coefficients obtained with the BILD method against the same quantities found by the SNOPT algorithm. The trends are very close to linear with average errors of less than 0.3% for the mentioned quantities. In Tab. 3, we present additional information for other key quantities of interest. The largest average errors occur for the total rate of energy loss (12.0%) and the norm of the blade chord distribution (12.4%). Collectively, the results presented in this section verify that the BILD method is able to predict the optimal blade geometry with reasonable accuracy as well as faster and more robustly, compared to numerical BEM optimization.

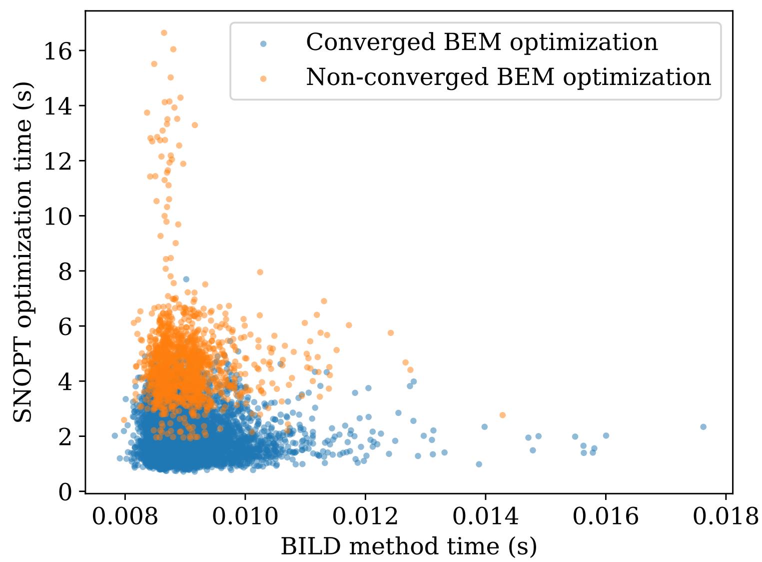

Figure 4: BILD method vs. BEM SNOPT optimization time

5.2 Parameter sweeps

5.2.1 Ideal rotor shape sweeps without root chord correction

In Fig. 6, we show 40 ideal rotor designs corresponding to four different operating conditions specified by advance ratio J, which varies from zero to three across the rows. In the first column, we plot the ideal chord distribution as a top-down view of the blade. In the second column, we plot

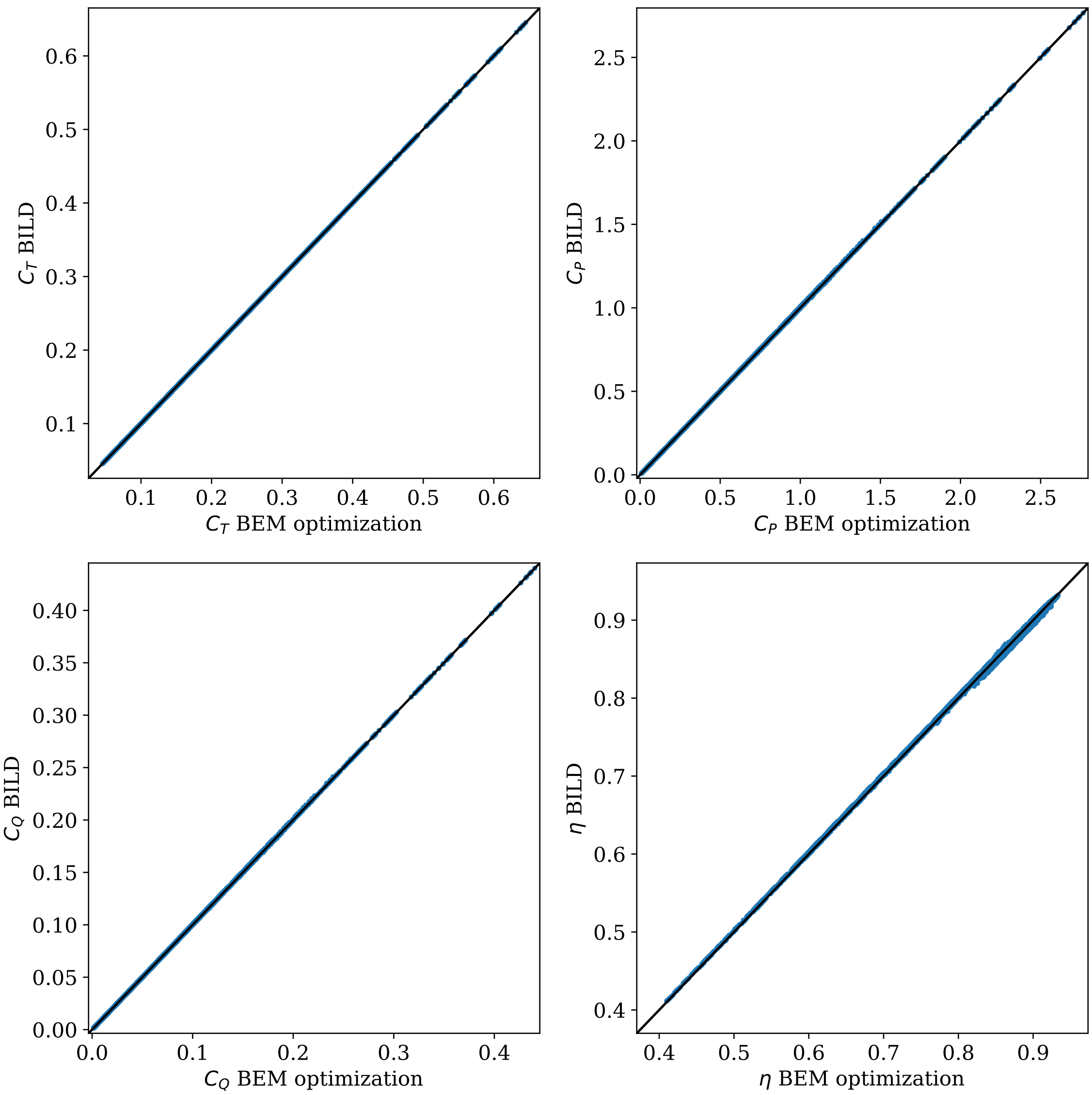

Figure 5: Performance metrics for 10,000 BILD model evaluations plotted against the same metrics obtained by a nonlinear programming algorithm.

the ideal blade twist distribution from root to tip. The different curves shown in gray represent different designs by varying the reference chord length c_r from 10 cm (black) to 40 cm (light gray) at a normalized reference radius of $r/R = 0.5$.

We see that the ideal blade shape in hover (i.e. $J = 0$) is noticeably different than that in forward flight. The maximum chord length is near the hub and the chord decreases (approximately linearly) toward the tip, where the chord is small. We see that the overall chord profile increases

Table 3: Summary of 10,000 numerical experiments

Quantity	BILD method	BEM optimization	Average relative error (%)
Thrust coefficient C_T [min, max]	[0.046, 0.645]	[0.046, 0.645]	6.337E-10
Torque coefficient C_Q [min, max]	[0.001, 0.440]	[0.001, 0.440]	0.161
Power coefficient C_P [min, max]	[0.009, 2.766]	[0.009, 2.766]	0.161
Efficiency η [min, max]	[0.412, 0.932]	[0.410, 0.933]	0.156
Figure of merit FM [min, max]	[0.691, 0.770]	[0.693, 0.770]	0.288
Rate of energy loss (kW) [min, max]	[0.087, 90.287]	[0.104, 116.932]	11.966
Blade twist distribution (norm)	–	–	3.583
Blade chord distribution (norm)	–	–	12.406
Percent converged	100	86.810	–
Average run time (s)	0.009	2.130	–

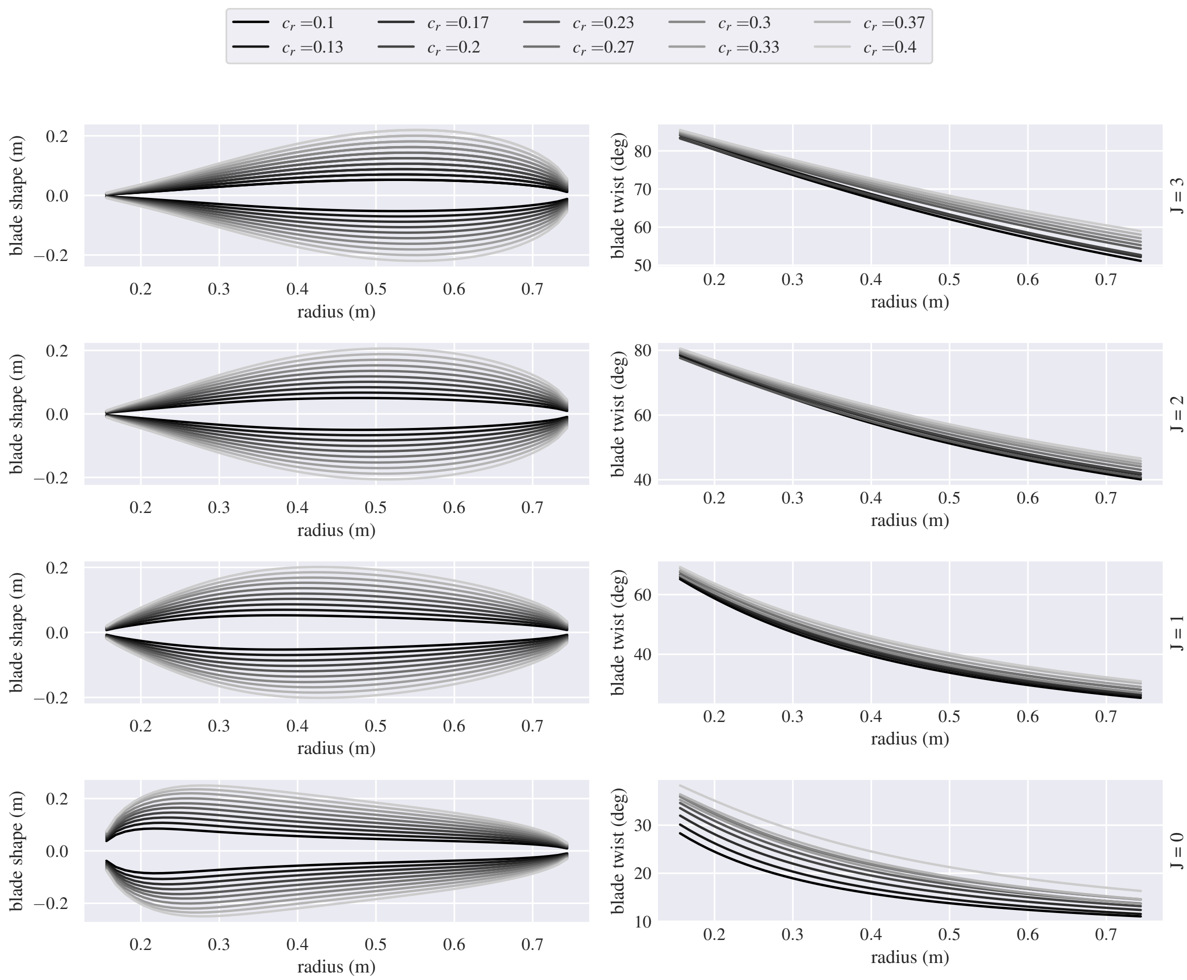

Figure 6: Ideal rotor blade geometries computed with the BILD method for different advance ratios J and reference chord lengths c_r

with the reference chord c_r, which is to be expected. In terms of the twist distribution, we see that the twist decreases from about 30 degrees at the root to between 10 and 20 degrees for zero advance ratio. The root and tip twist angles increase with the reference chord length c_r.

As we increase advance ratio J, the ideal rotor shape changes notably. The location of maximum chord length moves away from the hub as J increases and effectively becomes the value of the reference chord c_r. Similarly, the twist distribution also changes with J, with the blade being more twisted. A notable feature of blades designed for forward axial flight is that the chord becomes very small near the hub, which makes such a design not feasible. This also occurs for designs obtained with SNOPT BEM optimizations (see Fig. 11 in the Appendix) if no lower bound is placed on the chord length at the root.

5.2.2 Ideal rotor shape sweeps with root chord correction

In this section, we propose a solution to the problem of the infeasibly small root chord for forward flight. We adjust the chord distribution that we obtain from the back-computation step and take a weighted average of the reference chord c_r and the chord distribution from the back-computation, such that

$$c_{cor}^i = e^{-kr^i} c_r + \left(1 - e^{-kr^i}\right) c_{bc}^i \;\; i = 1, 2 \ldots, n, \tag{32}$$

where c_{cor} is the corrected chord, c_r is the reference chord, k is a constant, c_{bc} is the original back-computed value of the chord, and the superscript i denotes the radial station. We see that Eq. (32) corrects the chord near the root by weighting some fraction of the reference chord (determined by k) more heavily near the root and allows the chord profile to take its original form as we move away from the root. Figure 7 shows the effect of this correction method on the chord-distribution. We see that all rotor designs have a more reasonable chord length at the hub. It should be noted that this design change only affects the chord profile and not the twist profile.

To investigate how this modified geometry changes the aerodynamics of the rotor, we perform BEM simulations of the original and corrected designs for the same operating conditions and determine the percent change in key parameters such as thrust, torque, efficiency, and blade solidity. The results are shown in Appendix 7.3, Fig. 12. Here we plot the quantities of interest against

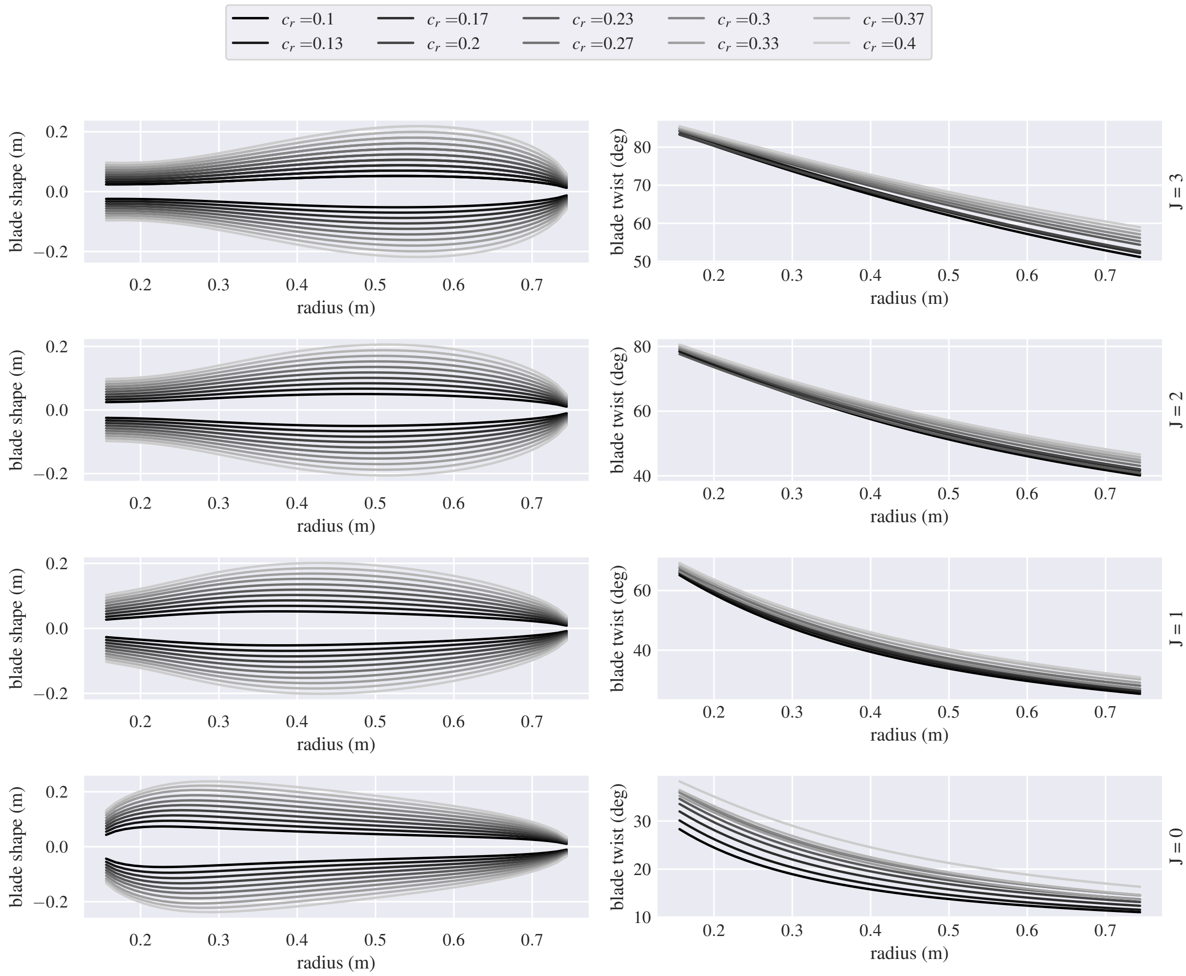

Figure 7: Ideal rotor blade geometries computed with the BILD method for different advance ratios J and reference chord lengths c_r, using the root-chord correction of Eq. (32)

different values of the reference chord length c_r at different operating conditions J, which we vary across the rows. The different curves on the subplots represent different reference radii. We see that the effect of correcting the thin root chord is most noticeable in blade solidity, which is expected. However, there is no significant change in the performance parameters (less than 5% for T and Q and less than 1% for efficiency η and figure of merit FM). This means that with the chord correction, the BILD method can compute optimal rotor designs for hover and forward flight.

5.2.3 Performance of ideal rotors

In Fig. 8, we present the performance of 280 rotors, designed with the BILD method. Each data point represents a different blade design. We plot T, Q, η, and FM against varying values of the reference chord length c_r. The different curves on each subplot represent varying normalized reference radii. The operating condition is specified by advance ratio and varied across subplot rows. All rotors were sized with a 1.5 m radius and three blades.

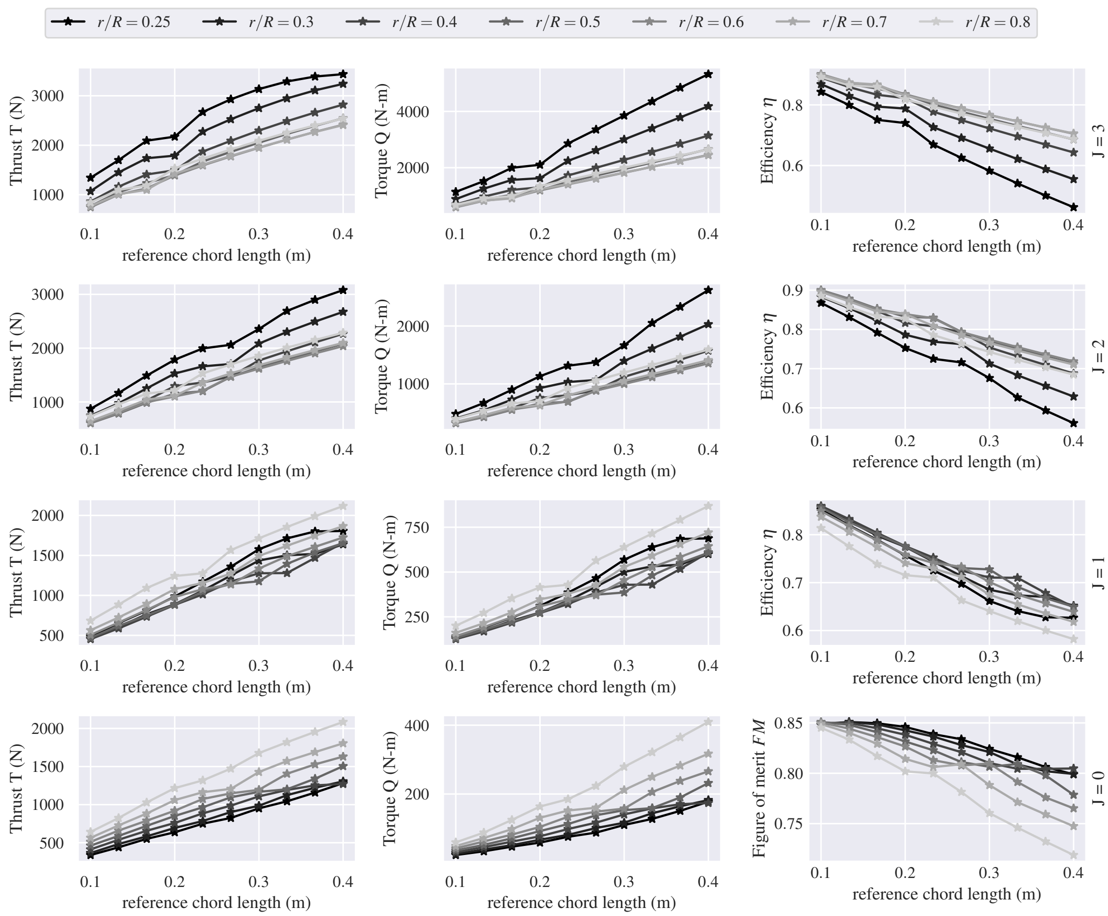

Figure 8: Rotor performance of 280 rotors designed using the BILD method

We see a clear correlation between the performance parameters and the reference chord. In general, rotors with higher blade solidity produce more thrust but also require higher torque, which leads to a decrease in efficiency. This trend is confirmed as thrust and torque increase (mostly linearly) with increasing reference chord lengths for all advance ratios. For efficiency, the opposite is true, where an increase in reference chord causes a decrease in efficiency and figure of merit in the hover case. Another observation is the fluctuating values of the quantities of interest. We attribute these fluctuations to imperfections in the airfoil surrogate model used in our BEM code (see Sec. 3.2). Figure 8 serves as a reference to gauge the effects of changing reference chord and radius along with advance ratio on rotor performance.

Lastly, in Fig. 9, we plot efficiency η against advance ratio J for four different ideal blade designs, computed with the BILD method for design operating conditions of $J_{des} = 0.5$, 1, 1.5, 2. We also show the corresponding blade chord and twist profiles, which we used as inputs to BEM analyses to produce the η vs. J curves.

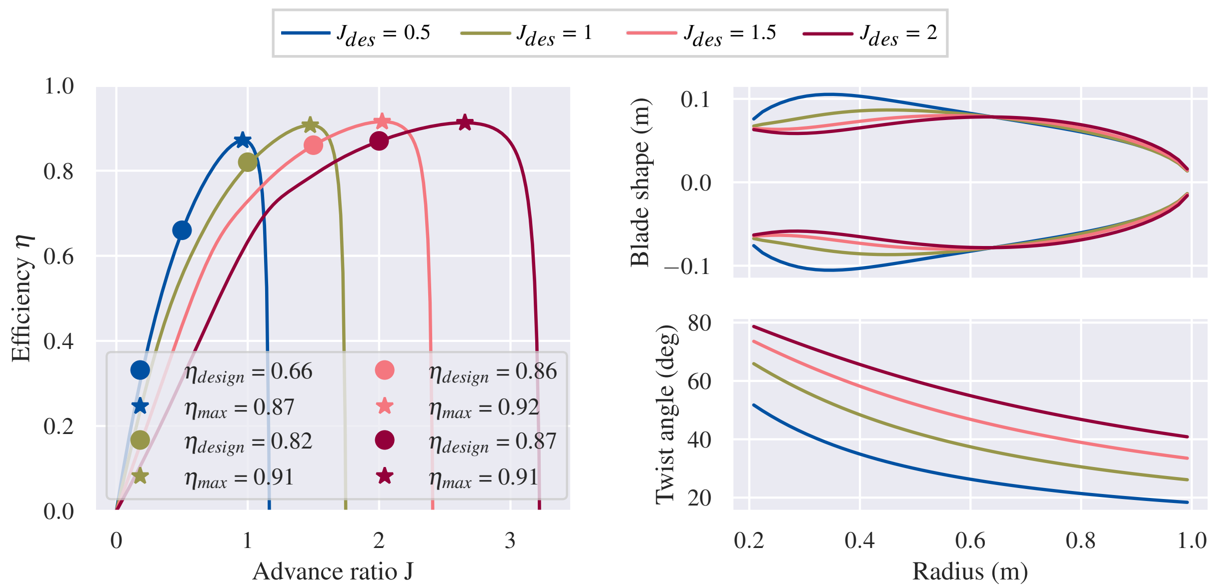

Figure 9: Efficiency η vs advance ratio J for different ideal rotor geometries

The goal is to investigate the sensitivity of blade designs produced with the BILD method to changes in operating conditions. The circle-shaped markers show the efficiency of the rotors at the design operating condition while the star-shaped markers show the maximum efficiency that is attainable with the given rotor design. We see that in all cases the maximum efficiency (over 80% for all rotors) is higher than the efficiency at the design operating condition.

This may seem unintuitive at first since the goal of the BILD method is to design rotors of maximum efficiency given an operating condition. However, this does not mean that the highest efficiency will be achieved at that operating condition. This is because the rotor performance is primarily dependent on our choice of the reference chord, reference radius, and the airfoil polar ($(C_l/C_d)_{max}$). From Fig. 8 we know that efficiency decreases with increasing reference chord. If we wanted to achieve maximum efficiency at the specified operating condition, we would have to solve an optimization problem in which the reference chord is a design variable. Another way to explain why the maximum efficiency is higher than the efficiency at the design operating condition is to consider the case $J_{des} = 0$ (i.e., an optimal design for hover). By definition, the efficiency is zero in hover. However, we can achieve some positive efficiency if we operated the same design for $J > 0$.

As stated before, the BILD method computes the optimal rotor geometry for a given operating condition, specified by advanced ratio. Changing the cruise velocity or rotational speed will result in a different blade design. It is therefore important to know how well a design computed with the BILD method performs under different operating conditions. Figure 9 can be used to evaluate the sensitivity of an optimal rotor design (in terms of efficiency) to a change in advance ratio. Rotors that are designed for higher advance ratios are less sensitive to a change in advance ratio. For instance, a rotor designed for $J_{des} = 2$ (dark red curve), can achieve an efficiency of over 80% when operating between $J \approx 1.5$ and $J \approx 3.1$. A rotor designed for $J_{des} = 0.5$ (blue curve) achieves an efficiency of 80% or higher on a smaller range, between $J \approx 0.7$ and $J \approx 1.1$. Knowing how sensitive a rotor is to a change in operating conditions is important in vehicle design.

6 Conclusion

Motivated by a renewed interest in rotary-wing aircraft due to the emergence of electrified propulsion, this paper presented a fast and robust design method for aerodynamically optimal rotors, called the BEM-based ideal-loading design (BILD) method. The method is based on blade element momentum theory and computes the optimal blade chord and twist distributions that minimize the aerodynamic losses for a given operating condition. To verify the BILD method, we conducted 10,000 numerical experiments in which we compared the results of the BILD method with those found by a state-of-the-art nonlinear programming algorithm. Based on the results, the BILD method can find the optimal rotor design over 200 times faster with relative errors of less than 0.3% for key aerodynamic performance metrics such as efficiency, thrust, torque, and power coefficient. In addition, the BILD method is provably convergent, and indeed converged in all cases considered, whereas the nonlinear programming algorithm only converged in 87% of the cases.

Despite these promising results, the BILD method has two main limitations. First, it only considers the aerodynamics of the rotor and does not take into account blade structural dynamics or acoustics, which are important disciplines in comprehensive rotor blade design. Second, the aerodynamic analysis is limited by the accuracy and applicability of blade element momentum theory. As such, the wake is not modeled and the effect of edgewise flow cannot be captured with reasonable accuracy.

The results of this paper suggest that for appropriate design scenarios, the BILD method is a viable option for fast first-order approximations of aerodynamically optimal rotor geometries. Such design scenarios may arise at the conceptual level for axial flow and in cases where blade dynamics are not modeled and acoustic constraints are not enforced. Examples of appropriate design scenarios are certain urban air mobility (UAM) concepts during cruise (e.g., Lift+Cruise) or military unmanned aerial vehicles (UAVs). In addition, due to its proven robustness and fast computation time, BILD may be embedded into large-scale multidisciplinary design optimization (MDO) studies of rotary-wing aircraft. A MDO tool that has received attention in the last couple of years is NASA's OpenMDAO framework [60], which uses gradient-based optimization algorithms to efficiently solve large-scale coupled systems. Two MDO investigations [61, 62] of electric aircraft using OpenMDAO have been done in which the rotor aerodynamics was modeled using BEM theory and the blade geometry was optimized numerically. Performing blade shape optimization with the BILD method can potentially speed up the system-level optimization.

In terms of future work, a comparison of BILD with the well-established minimum-induced loss (MIL) design method can provide insights into the strengths and limitations of both methods in terms of the underlying theory, computational efficiency, and robustness. Other areas of future work include the integration of BILD into large-scale MDO studies, the exploration of other application domains such as wind energy and hydrodynamics, and extending the BILD algorithm to allow for multiple airfoils along the rotor span. For the results shown in this paper, a single airfoil was used.

While the underlying theory of BILD allows for multiple airfoils, verification is needed to ensure that the designs remain optimal.

Acknowledgments

This work was supported, in part, by NASA Grant No. 80NSSC21M0070.

7 Appendix

7.1 Positivity of the ideal-loading constant λ

We briefly show that given Assumption 3, the ideal-loading constant is strictly positive. The expression for λ is

$$\lambda = \frac{V_\theta u_\theta}{2\left(2u_x - V_x\right)} + \frac{V_\theta u_x}{V_\theta - u_\theta} - V_x.$$

The first term is greater than zero, that is

$$0 < \frac{V_\theta u_\theta}{2\left(2u_x - V_x\right)}.$$

This implies that λ is greater than the last two terms, such that

$$\lambda > \frac{V_\theta u_x}{V_\theta - u_\theta} - V_x.$$

Since the term $V_\theta/(V_\theta - u_\theta) > 1$, we can remove it and maintain the inequality, which leads to

$$\lambda > u_x - V_x > 0.$$

7.2 Supplemental equations

Equation (33) shows the piecewise formulation of the lift and drag coefficient for a single Reynolds number case. This formulation is repeated based on XFOIL data for a total of ten Reynolds numbers ranging from 5x10^4 to 2x10^6. The raw XFOIL data is interpolated such that within the stall regime, the lift coefficient is modeled linearly with α and the drag coefficient is interpolated with a fourth order polynomial. Cubic smoothing is applied in the tranision region and the Viterna [19] method is applied in the post-stall region to extrapolate to $\pm 90°$. Once the data is properly interpolated for each Reynolds number case, two surrogate models are trained for C_l and C_d as a function of Reynolds number and angle of attack.

$$C_l(\alpha)\Big|_{Re=const.} = \begin{cases} C_{l_0} + C_{l_\alpha}\alpha & \alpha \le \alpha_{stall} - \epsilon \\ c_3\alpha^3 + c_2\alpha^2 + c_1\alpha + c_0, & \alpha_{stall} - \epsilon \le \alpha \le \alpha_{stall} + \epsilon \\ A_1 \sin 2\alpha + A_2 \frac{\cos^2\alpha}{\sin\alpha}, & \alpha \ge \alpha_{stall} + \epsilon \end{cases}, \tag{33a}$$

$$C_d(\alpha)\Big|_{Re=const.} = \begin{cases} a_4\alpha^4 + a_3\alpha^3 + a_2\alpha^2 + a_1\alpha + a_0, & \alpha \leq \alpha_{stall} - \epsilon \\ d_3\alpha^3 + d_2\alpha^2 + d_1\alpha + d_0, & \alpha_{stall} - \epsilon \leq \alpha \leq \alpha_{stall} + \epsilon \\ B_1 \sin^2\alpha + B_2\cos\alpha, & \alpha \geq \alpha_{stall} + \epsilon \end{cases}, \tag{33b}$$

where the smoothing region is confined to $\epsilon = \pm 1.5°$ and the Viterna coefficients A_1, A_2, B_1, B_2 can be found in [19]. Smoothing is necessary to avoid training the surrogate model on noisy data and to avoid local optima during optimization.

Equation (34) repeats Eq. (27) presented in Sec. 4.2, including the polynomial coefficients. The coefficients are expressed in terms of advance ratio J ($J = {}^{V_x\pi}/_{V_\theta}$), lift-to-drag ratio (${}^{L}/_{D}$) and the ideal-loading constant λ.

$$\begin{aligned}
&P(\eta_2) = a_4{\eta_2}^4 + a_3\eta_2^3 + a_2\eta_2^2 + a_1\eta_2 + a_0 = 0,\\
&\qquad \text{where}\\
&a_0 = -4\pi^6 + \frac{8\pi^6}{(L/D)^2} + 4J^2\pi^4 + 8J^4\ \pi^2 + \frac{\lambda^2J^2\pi^4}{V_\theta^2} + \frac{6\lambda J^3\pi^3}{V_\theta} - \frac{4\lambda\pi^6}{(L/D)\,V_\theta} - \frac{20J\pi^5}{(L/D)} -\\
&\qquad \frac{20J^3\pi^3}{(L/D)} + \frac{8J^2\pi^4}{(L/D)^2} - \frac{14\lambda J^2\pi^4}{(L/D)\,V_\theta} - \frac{2\lambda^2J\pi^5}{(L/D)\,V_\theta^2} + \frac{4\lambda J\pi^5}{(L/D)^2\,V_\theta}\\
&a_1 = 40\pi^6 - \frac{24\pi^6}{(L/D)^2} + \frac{4\lambda^2\pi^6}{V_\theta^2} + 16J^2\pi^4 - 24J^4\pi^2 - \frac{4\lambda^2J^2\pi^4}{V_\theta^2} + \frac{24\lambda J\pi^5}{V_\theta} - \frac{20\lambda J^3\pi^3}{V_\theta} +\\
&\qquad \frac{12\lambda\pi^6}{(L/D)\,V_\theta} + \frac{84J\pi^5}{(L/D)} + \frac{84J^3\pi^3}{(L/D)} - \frac{24J^2\pi^4}{(L/D)^2} + \frac{68\lambda J^2\pi^4}{(L/D)\,V_\theta} + \frac{12\lambda^2J\pi^5}{(L/D)\,V_\theta^2} - \frac{16\lambda J\pi^5}{(L/D)^2\,V_\theta}\\
&a_2 = -132\pi^6 + \frac{16\pi^6}{(L/D)^2} - \frac{20\lambda^2\pi^6}{V_\theta^2} - 116J^2\pi^4 + 16J^4\pi^2 + \frac{4\lambda^2J^2\pi^4}{V_\theta^2} - \frac{104\lambda J\pi^5}{V_\theta} + \frac{16\lambda J^3\pi^3}{V_\theta} -\\
&\qquad \frac{8\lambda\pi^6}{(L/D)\,V_\theta} - \frac{128J\pi^5}{(L/D)} - \frac{128J^3\pi^3}{(L/D)} + \frac{16J^2\pi^4}{(L/D)^2} - \frac{112\lambda J^2\pi^4}{(L/D)\,V_\theta} - \frac{24\lambda^2J\pi^5}{(L/D)\,V_\theta^5} + \frac{16\lambda J\pi^5}{(L/D)^2\,V_\theta}\\
&a_3 = 160\pi^6 + \frac{32\lambda^2\pi^6}{V_\theta^2} + 160J^2\pi^4 + \frac{144\lambda J\pi^5}{V_\theta} + \frac{64J\pi^5}{(L/D)} + \frac{64J^3\pi^3}{(L/D)} + \frac{64\lambda J^2\pi^4}{(L/D)\,V_\theta} + \frac{16\lambda^2J\pi^5}{(L/D)\,V_\theta^2}\\
&a_4 = -64\pi^6 - 64J^2\pi^4 - \frac{16\lambda^2\pi^6}{V_\theta^2} - \frac{64\lambda J\pi^5}{V_\theta}
\end{aligned} \tag{34}$$

Equation (35) is a special case of the quartic equation (34), when $V_x = 0$. It is clear that $\eta_2 = 1$ is a solution.

$$P(V_x=0) = -4V_\theta\left(\eta_2-1\right)\Big[\left(4\lambda^2+16V_\theta^2\right)\eta_2^3-\left(4\lambda^2+24V_\theta^2\right)\eta_2^2+ \left(\lambda^2+9V_\theta^2-\frac{4V_\theta^2}{\left(L/D\right)^2}+\frac{2V_\theta\lambda}{L/D}\right)\eta_2-V_\theta^2+\frac{2V_\theta^2}{\left(L/D\right)^2}-\frac{V_\theta\lambda}{L/D}\Big] \tag{35}$$

Equation (36) shows the expression for the second real root of (35). Recall that the first real root is $\eta_2 = 1$.

$$\begin{aligned}
&\eta_2 = A + B + \frac{d}{B},\\
&\text{where}\\
&A = \frac{\lambda^2 + 6\,{V_\theta}^2}{3\,\lambda^2 + 12\,{V_\theta}^2}\\
&B = \left(a + \sqrt{\left(a+b-c\right)^2 - d^3} + b - c\right)^{\frac{1}{3}}\\
&\quad\text{where}\\
&\quad a = \frac{0.1250\,V_\theta\left(V_\theta\left(L/D\right)^2 + \lambda\,\left(L/D\right) - 2\,V_\theta\right)}{\left(L/D\right)^2\left(\lambda^2 + 4\,{V_\theta}^2\right)}\\
&\quad b = \frac{0.0370\left(\lambda^2 + 6\,{V_\theta}^2\right)^3}{\left(\lambda^2 + 4\,{V_\theta}^2\right)^3}\\
&\quad c = \frac{0.0417\left(\lambda^2 + 6\,{V_\theta}^2\right)\left(\left(L/D\right)^2\lambda^2 + 9\left(L/D\right)^2{V_\theta}^2 + 2\,\left(L/D\right)\,\lambda\,V_\theta - 4\,{V_\theta}^2\right)}{\left(L/D\right)^2\left(\lambda^2 + 4\,{V_\theta}^2\right)^2}\\
&\quad d = \frac{0.0278\left(\begin{smallmatrix}\left(L/D\right)^2\lambda^4 + 9\left(L/D\right)^2\lambda^2{V_\theta}^2 + 36\left(L/D\right)^2{V_\theta}^4 - 6\left(L/D\right)\lambda^3V_\theta -\\ 24\left(L/D\right)\lambda{V_\theta}^3 + 12\,\lambda^2{V_\theta}^2 + 48\,{V_\theta}^4\end{smallmatrix}\right)}{\left(L/D\right)^2\left(\lambda^2 + 4\,{V_\theta}^2\right)^2}
\end{aligned} \tag{36}$$

7.3 Supporting Figures

Figure 10 shows the sensitivity of the normalized axial induced velocity u_x (see Eq. (26)) as a function of the lift-to-drag ratio for for different values of V_x, V_θ, and η_2.

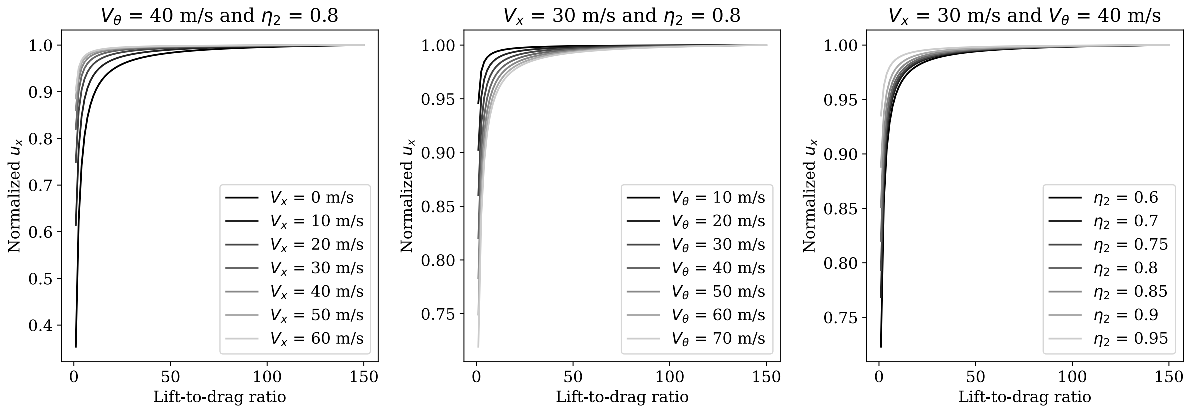

Figure 10: Normalized u_x vs. lift-to-drag ratio for different values of V_x, V_θ, and η_2.

Figure 11 shows additional blade profiles similar to Fig. 3, obtained with the BILD method and the SNOPT BEM optimization, for advance ratios of $J > 0$. We see that the small chord length at the root also occurs for the SNOPT BEM optimization for larger values of advance ratios.

Figure 12 shows the effect of the root-chord correction technique proposed in section 5.2.2. It is clear that the change in thrust, torque and efficiency is negligibly small. The biggest effect is the increase in blade solidity, which is expected. We believe that the fluctuations in some of the subplots are due to imperfections due to the airfoil surrogate model (see Sec. 3.2).

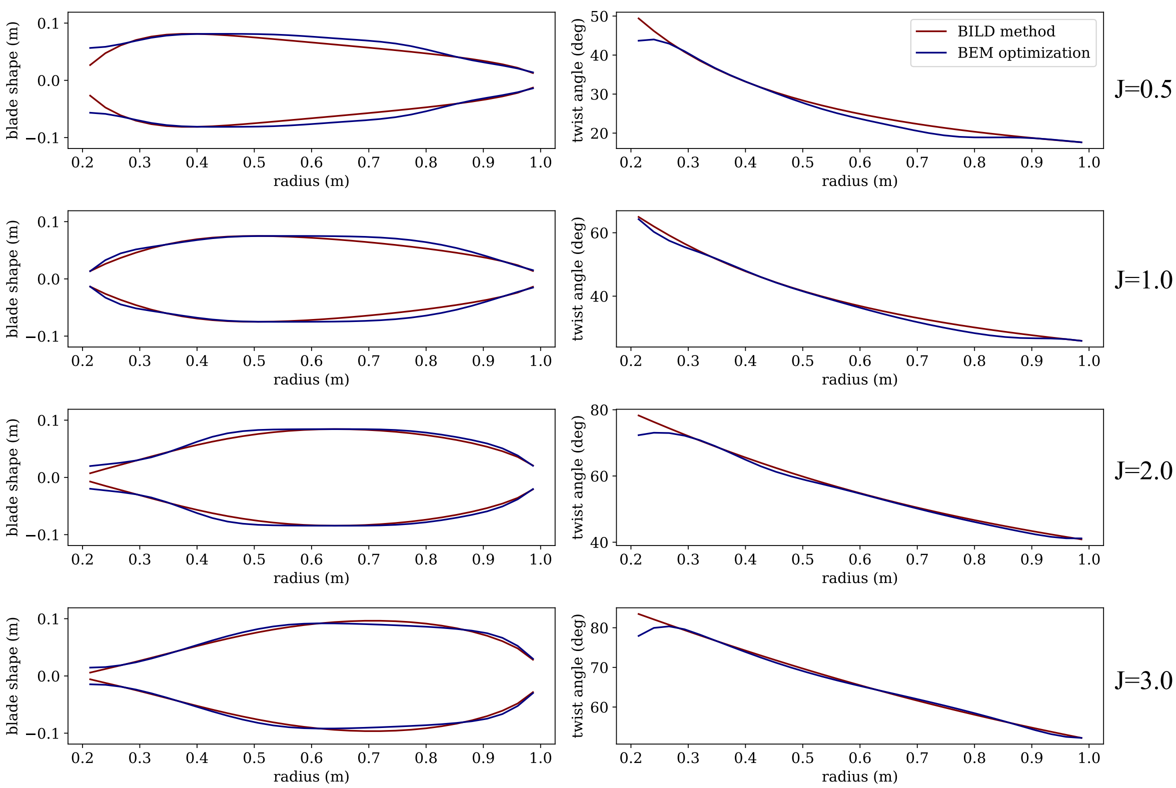

Figure 11: Blade geometries obtained with BEM optimization and BILD for $J > 0$

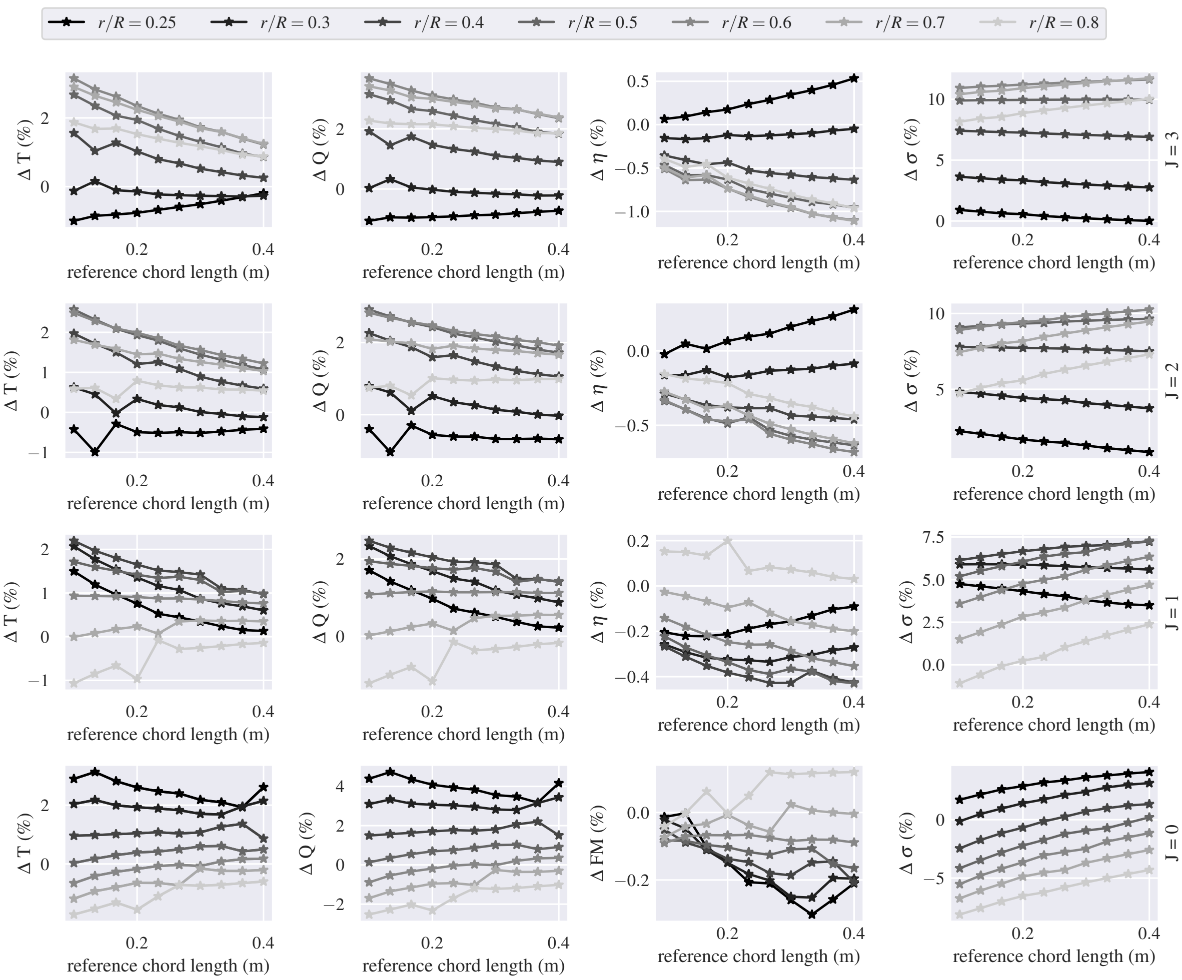

Figure 12: Percent change in T, Q, η and σ due to root-chord correction

References

[1] Shahab Hasan. *Urban air mobility (UAM) market study*. Tech. rep. 2019.

[2] Rohit Goyal, Colleen Reiche, Chris Fernando, Jacquie Serrao, Shawn Kimmel, Adam Cohen, and Susan Shaheen. *Urban air mobility (UAM) market study*. Tech. rep. 2018.

[3] Christopher Silva, Wayne R Johnson, Eduardo Solis, Michael D Patterson, and Kevin R Antcliff. "VTOL urban air mobility concept vehicles for technology development". In: *2018 Aviation Technology, Integration, and Operations Conference*. 2018, p. 3847.

[4] Helge Aa Madsen, Christian Bak, Mads Døssing, Robert Mikkelsen, and Stig Øye. "Validation and modification of the Blade Element Momentum theory based on comparisons with actuator disc simulations". In: *Wind Energy: An International Journal for Progress and Applications in Wind Power Conversion Technology* 13.4 (2010), pp. 373–389.

[5] H Aa Madsen, R Mikkelsen, Stig Øye, C Bak, and Jeppe Johansen. "A Detailed investigation of the Blade Element Momentum (BEM) model based on analytical and numerical results and proposal for modifications of the BEM model". In: *Journal of Physics: Conference Series*. Vol. 75. 1. IOP Publishing. 2007, p. 012016.

[6] Ohad Gur and Aviv Rosen. "Comparison between blade-element models of propellers". In: *The Aeronautical Journal* 112.1138 (2008), pp. 689–704.

[7] R Bontempo and M Manna. "Analysis and evaluation of the momentum theory errors as applied to propellers". In: *AIAA Journal* 54.12 (2016), pp. 3840–3848.

[8] Rodolfo Bontempo and Marcello Manna. "Effects of the approximations embodied in the momentum theory as applied to the nrel phase vi wind turbine". In: *International Journal of Turbomachinery, Propulsion and Power* 2.2 (2017), p. 9.

[9] R Bontempo and M Manna. "Highly accurate error estimate of the momentum theory as applied to wind turbines". In: *Wind Energy* 20.8 (2017), pp. 1405–1419.

[10] Rodolfo Bontempo and Marcello Manna. “Verification of the axial momentum theory for propellers with a uniform load distribution”. In: *International Journal of Turbomachinery, Propulsion and Power* 4.2 (2019), p. 8.

[11] Hermann Glauert. “Airplane propellers”. In: *Aerodynamic theory*. Springer, 1935, pp. 169–360.

[12] Wen Zhong Shen, Robert Mikkelsen, Jens Nørkær Sørensen, and Christian Bak. “Tip loss corrections for wind turbine computations”. In: *Wind Energy: An International Journal for Progress and Applications in Wind Power Conversion Technology* 8.4 (2005), pp. 457–475.

[13] Emmanuel Branlard and Mac Gaunaa. “Development of new tip-loss corrections based on vortex theory and vortex methods”. In: *Journal of Physics: Conference Series*. Vol. 555. 1. IOP Publishing. 2014, p. 012012.

[14] Rens MacNeill and Dries Verstraete. “Blade element momentum theory extended to model low Reynolds number propeller performance”. In: *The Aeronautical Journal* 121.1240 (2017), pp. 835–857.

[15] Ohad Gur and Aviv Rosen. “Propeller performance at low advance ratio”. In: *Journal of aircraft* 42.2 (2005), pp. 435–441.

[16] John Brandt and Michael Selig. “Propeller performance data at low reynolds numbers”. In: *49th AIAA Aerospace Sciences Meeting including the New Horizons Forum and Aerospace Exposition*. 2011, p. 1255.

[17] James Tangler and David Kocurek. “Wind turbine post-stall airfoil performance characteristics guidelines for blade-element momentum methods”. In: *43rd AIAA Aerospace Sciences Meeting and Exhibit*. 2005, p. 591.

[18] Stephen A Whitmore and Robert S Merrill. “Nonlinear large angle solutions of the blade element momentum theory propeller equations”. In: *Journal of Aircraft* 49.4 (2012), pp. 1126–1134.

[19] Faisal Mahmuddin, Syerly Klara, Husni Sitepu, and Surya Hariyanto. "Airfoil lift and drag extrapolation with viterna and montgomerie methods". In: *Energy Procedia* 105 (2017), pp. 811–816.

[20] Björn Montgomerie. "Methods for root effects, tip effects and extending the angle of attack range to {+-} 180 deg., with application to aerodynamics for blades on wind turbines and propellers". In: (2004).

[21] Curran Crawford. "Re-examining the precepts of the blade element momentum theory for coning rotors". In: *Wind Energy: An International Journal for Progress and Applications in Wind Power Conversion Technology* 9.5 (2006), pp. 457–478.

[22] Manelisi Kagame Rwigema. "Propeller blade element momentum theory with vortex wake deflection". In: *27th International congress of the aeronautical sciences*. Vol. 2010. 2010, pp. 2–3.

[23] Leonardus Louis Maria Veldhuis. "Propeller wing aerodynamic interference". In: (2005).

[24] John T Conway. "Analytical solutions for the actuator disk with variable radial distribution of load". In: *Journal of Fluid Mechanics* 297 (1995), pp. 327–355.

[25] Andrew Ning, Gregory Hayman, Rick Damiani, and Jason M Jonkman. "Development and validation of a new blade element momentum skewed-wake model within AeroDyn". In: *33rd Wind Energy Symposium*. 2015, p. 0215.

[26] Zhenye Sun, Wen Zhong Shen, Jin Chen, and Wei Jun Zhu. "Improved fixed point iterative method for blade element momentum computations". In: *Wind Energy* 20.9 (2017), pp. 1585–1600.

[27] Ian Masters, JC Chapman, MR Willis, and JAC Orme. "A robust blade element momentum theory model for tidal stream turbines including tip and hub loss corrections". In: *Journal of Marine Engineering & Technology* 10.1 (2011), pp. 25–35.

[28] S Andrew Ning. "A simple solution method for the blade element momentum equations with guaranteed convergence". In: *Wind Energy* 17.9 (2014), pp. 1327–1345.

[29] Andrew Ning. “Using blade element momentum methods with gradient-based design optimization”. In: *Structural and Multidisciplinary Optimization* (2021), pp. 1–24.

[30] Albert Betz. “Schraubenpropeller mit geringstem Energieverlust”. In: *Gottinger Nachrichten* (1919), pp. 193–213.

[31] T Theodorsen. “Theory of Propellers. New York. McGraw-Hill”. In: (1948).

[32] E Eugene Larrabee. “Practical design of minimum induced loss propellers”. In: *SAE Transactions* (1979), pp. 2053–2062.

[33] Charles N Adkins and Robert H Liebeck. “Design of optimum propellers”. In: *Journal of Propulsion and Power* 10.5 (1994), pp. 676–682.

[34] Quentin R Wald. “The aerodynamics of propellers”. In: *Progress in Aerospace Sciences* 42.2 (2006), pp. 85–128.

[35] Martin Hepperle. “Inverse aerodynamic design procedure for propellers having a prescribed chord-length distribution”. In: *Journal of aircraft* 47.6 (2010), pp. 1867–1872.

[36] Lance W Traub. “Inverse propeller design for a prescribed chord or blade angle”. In: *Journal of Aircraft* 54.2 (2017), pp. 825–830.

[37] LW Traub. “Simplified propeller analysis and design including effects of stall”. In: *The Aeronautical Journal* 120.1227 (2016), pp. 796–818.

[38] Lance W Traub. “Considerations in Optimal Propeller Design”. In: *Journal of Aircraft* (2021), pp. 1–8.

[39] Robert E Davidson. “Optimization and performance calculation of dual-rotation propellers”. In: (1981).

[40] Sven Albert, Philipp Epple, Bettina Willinger, and Antonio Delgado. “High Efficiency Propeller Design Based on the Betz Minimum Induced Loss Condition and CFD Validation on an APC 8 Propeller”. In: *ASME International Mechanical Engineering Congress and Exposition.* Vol. 56321. American Society of Mechanical Engineers. 2013, V07BT08A052.

[41] Christopher Noel Hunter Lock, RC Pankhurst, and RG Fowler. *Determination of the Optimum Twist of an Airscrew Blade by the" calculus of Variations"*. HM Stationery Office, 1942.

[42] T Moriya. "Formulae for Propeller Characteristics Calculation and a Method to Obtain the Best Pitch Distribution". In: *Selected Scientific and Technical Papers* (1938), pp. 43–47.

[43] Johann Dorfling and Kamran Rokhsaz. "Constrained and unconstrained propeller blade optimization". In: *Journal of Aircraft* 52.4 (2015), pp. 1179–1188.

[44] Li Ko Chang and John P Sullivan. "Optimization of propeller blade twist by an analytical method". In: *AIAA journal* 22.2 (1984), pp. 252–255.

[45] Anthony V Fiacco and Garth P McCormick. *Nonlinear programming: sequential unconstrained minimization techniques.* SIAM, 1990.

[46] Li Ko Chang and George L Stefko. *Application of an optimization method to high performance propeller designs.* Lewis Research Center, 1984.

[47] Jinsoo Cho and Seung-Chul Lee. "Propeller blade shape optimization for efficiency improvement". In: *Computers & fluids* 27.3 (1998), pp. 407–419.

[48] Christoph Burger, Roy Hartfield, and John Burkhalter. "Propeller Performance Optimization using Vortex Lattice Theory and a Genetic Algorithm". In: *44th AIAA Aerospace Sciences Meeting and Exhibit.* 2006, p. 1067.

[49] Marius L Ruh and John T Hwang. "Robust modeling and optimal design of rotors using blade element momentum theory". In: *AIAA AVIATION 2021 FORUM.* 2021, p. 2598.

[50] John T Hwang and Joaquim RRA Martins. "A fast-prediction surrogate model for large datasets". In: *Aerospace Science and Technology* 75 (2018), pp. 74–87.

[51] Mohamed Amine Bouhlel, John T Hwang, Nathalie Bartoli, Rémi Lafage, Joseph Morlier, and Joaquim RRA Martins. "A Python surrogate modeling framework with derivatives". In: *Advances in Engineering Software* 135 (2019), p. 102662.

[52] Mark Drela. “XFOIL: An analysis and design system for low Reynolds number airfoils”. In: *Low Reynolds number aerodynamics*. Springer, 1989, pp. 1–12.

[53] Izrail Moiseevitch Gelfand, Richard A Silverman, et al. *Calculus of variations*. Courier Corporation, 2000.

[54] Robert Weinstock. *Calculus of variations: with applications to physics and engineering*. Courier Corporation, 1974.

[55] Louis Komzsik. *Applied calculus of variations for engineers*. CRC Press, 2018.

[56] Magnus Rudolph Hestenes. *Calculus of variations and optimal control theory*. Wiley, 1966.

[57] Philip E Gill, Walter Murray, and Michael A Saunders. “SNOPT: An SQP algorithm for large-scale constrained optimization”. In: *SIAM review* 47.1 (2005), pp. 99–131.

[58] Nicholas Polaczyk, Enzo Trombino, Peng Wei, and Mihaela Mitici. “A review of current technology and research in urban on-demand air mobility applications”. In: *8th Biennial Autonomous VTOL Technical Meeting and 6th Annual Electric VTOL Symposium*. 2019, pp. 333–343.

[59] Shamsheer S Chauhan and Joaquim RRA Martins. “Tilt-wing eVTOL takeoff trajectory optimization”. In: *Journal of Aircraft* 57.1 (2020), pp. 93–112.

[60] Justin S Gray, John T Hwang, Joaquim RRA Martins, Kenneth T Moore, and Bret A Naylor. “OpenMDAO: An open-source framework for multidisciplinary design, analysis, and optimization”. In: *Structural and Multidisciplinary Optimization* 59.4 (2019), pp. 1075–1104.

[61] John T Hwang and Andrew Ning. “Large-scale multidisciplinary optimization of an electric aircraft for on-demand mobility”. In: *2018 AIAA/ASCE/AHS/ASC Structures, Structural Dynamics, and Materials Conference*. 2018, p. 1384.

[62] Tae Hyun Ha. *System-level performance investigation of eVTOL concepts using large-scale DEP-focused design optimizations*. University of California, San Diego, 2020.